

**EXTENSIONAL VISCOSITY OF HIGHLY ALIGNED DISCONTINUOUS
FIBER COMPOSITES IN STRETCH FORMING PROCESSES**

by

Henry Fidlow

A thesis submitted to the Faculty of the University of Delaware in partial fulfillment of the requirements for the degree of Honors Degree in Mechanical Engineering with Distinction


Spring 2022

© 2022 Henry Fidlow
All Rights Reserved

**EXTENSIONAL VISCOSITY OF HIGHLY ALIGNED DISCONTINUOUS
FIBER COMPOSITES IN STRETCH FORMING PROCESSES**

by

Henry Fidlow

Approved:  _____

Suresh G. Advani, Ph.D.
Professor in charge of thesis on behalf of the Advisory Committee

Approved:  _____

Thomas A. Cender, Ph.D.
Co-Advisor from the Center for Composite Materials

Approved:  _____

Antony N. Beris, Ph.D.
Committee member from the Department of Chemical and Biomolecular
Engineering

Approved:  _____

X. Lucas Lu, Ph.D.
Committee member from the Board of Senior Thesis Readers

Approved: _____
Michael Chajes, Ph.D.
Dean, University Honors Program

ACKNOWLEDGMENTS

I would like to thank Prof. Advani and Dr. Cender for all their help throughout the duration of my research with the Center of Composite Materials. Their help has been instrumental in providing me in-depth exposure to a variety of academic research avenues and the opportunity to work on this project has been a very enjoyable endeavor. I would also like to thank the rest of my thesis committee for their help throughout this process, as well as the faculty and staff at the Center for Composite Materials and Department of Mechanical Engineering. Lastly, thank you to my friends and family for their motivation and support. All these individuals have helped provide me with an excellent undergraduate experience.

This material is based upon work supported by the National Aeronautics and Space Administration under Grant and Cooperative Agreement No. 80NSSC20M0164, issued through the Aeronautics Research Mission Directorate, Transformative Aeronautics Concepts Program, University Leadership Initiative.

TABLE OF CONTENTS

LIST OF TABLES	vi
LIST OF FIGURES	vii
ABSTRACT	ix
1 INTRODUCTION	1
2 EXPERIMENTAL METHODOLOGY	4
2.1 TuFF Sample Preparation	4
2.2 PEI Rheology	5
2.3 Extensional Viscosity Testing	6
3 PREDICTIVE MICROMECHANICS MODEL	7
3.1 Shape Factor	8
3.2 Model Set Up	8
3.3 Newtonian Unit Cell Model	9
3.4 Shear Thinning Unit Cell Model	11
3.5 Applying Newtonian and Shear Thinning Regimes	12
4 POLYMER CHARACTERIZATION	13
4.1 Rheology Data	13
4.2 Time-Temperature Superposition (TTS)	14
5 EXTENSIONAL VISCOSITY	16
5.1 Viscous Behavior	16
5.2 Digital Image Correlation (DIC)	17
5.3 Temperature and Strain Rate Dependence	21
5.4 Repeatability	22
5.5 Test Data	23
5.6 Application of Predictive Model	24
6 DISCUSSION	26
6.1 Model Accuracy	26
6.1.1 Shear Thinning Behavior	26
6.1.2 Newtonian Plateau	27
6.2 Revised Model Prediction	29

7	CONCLUSIONS	31
	NOMENCLATURE	33
	REFERENCES	35
A	APPENDIX	36

LIST OF TABLES

Table 1. List of polymer shift factors derived from time-temperature superposition using a baseline temperature of 330°C.....	14
Table 2. List of ULTEM 1000 PEI material parameters for the Spriggs and Carreau-Yasuda models at 330°C.....	15

LIST OF FIGURES

Figure 1. (Left) TuFF fiber scale microstructure [3]. (Center) Cross-section of TuFF laminate structure. (Right) Stretch formed TuFF part [7].	2
Figure 2. Cross-sectional view of two neighboring unit cells, each consisting of a single fiber of radius R_i encompassed by a polymer of thickness $R_o - R_i$. Assuming perfect alignment and longitudinal packing, unit cell fiber volume fraction is computed.....	7
Figure 3. Shape factors for three different unit cell cross-sections. The fiber and resin are shown in dark and light gray respectively.	8
Figure 4. Front view of two neighboring cells. Velocity profile, v_z , is displayed relative to a symmetric neutral axis, $z = 0$, corresponding to a vertical distance of $L/4$ from either fiber end. The boundary conditions at the fiber and unit cell surfaces are $v_z(r = R_o) = 0$ and $v_z(r = R_i) = \pm \frac{\varepsilon_L L}{4}$ respectively.	9
Figure 5. Tensile stress is applied normally to the unit cell of interest, hence acting on an area of $A_\sigma = \pi R_o^2$. In the other direction, shear stress acts on the fiber surface, with area $A_\tau = \pi R_i L$. From these, a force balance can be conducted in the z -direction.	11
Figure 6. Polymer rheology data for five temperatures under a oscillatory frequency sweep.	13
Figure 7. Master curve constructed with time-temperature superposition (TTS) from experimental data shown alongside a Spriggs model.	15
Figure 8. Stress and viscosity versus strain for a sample under baseline conditions of 330°C and 0.001 s^{-1} . As seen in blue, stress relaxes to zero when stretching stops. This suggests the composite behaves viscously.	17
Figure 9. Visualization of gauge section determined using DIC methods. Sample dimensions were $L_o = 3''$ and $w_o = 1''$, whereas gauge section dimensions were $L_{gauge} = 1''$ and $w_{gauge} = 0.4''$	18
Figure 10. Evolution of local surface strain with average gauge strain using DIC methods for a single test at 350°C and 0.0002 s^{-1} . Using a scale from zero strain to $1.5\varepsilon_{gauge}$, minimal localization is observed.	19
Figure 11. Variability in gauge section strain for a single test at 330°C and 0.001s^{-1} ..	20

Figure 12. a) All seven tests under baseline conditions of 330°C and 0.001 s ⁻¹ . b) Viscosity dependence on strain rate and strain using a logarithmic scale.	211
Figure 13. a) Raw viscosity data for three temperatures at strain rates from 0.00005 s ⁻¹ to 0.01 s ⁻¹ . Error bars indicate ±2 standard deviations in both strain rate and viscosity across identical test conditions. b) Composite master curve after applying polymer shift factors.	23
Figure 14. (Top) Sample and DIC strain map for a failing sample stretched at 5*10 ⁻² s ⁻¹ . The jagged break in the speckle pattern indicates tearing. This is mirrored by the strain localization across the sample surface shown in the DIC strain map. (Bottom) Sample and DIC strain map for a passing sample stretched at 10 ⁻³ s ⁻¹ . The uniform DIC pattern indicates that tearing did not occur.	24
Figure 15. Piecewise model prediction applied to TuFF data in the Newtonian (blue) and shear thinning (red) regimes.	25
Figure 16. Revised model to incorporate a power law approximation that aligns with the behavior observed in the composite. The solid lines indicate the region within which forming rates are observed. The better alignment between the new region and the Carreau fit indicates improved model input accuracy.	27
Figure 17. (Left) Histogram of local volume fraction data. Data fits a normal distribution centered at $V_f = 58\%$ with a standard deviation of 8%. (Right) Colormap of local fiber volume fraction across a deconsolidated sample from microscopy.	28
Figure 18. Model predictions compared to TuFF data for varying fiber volume fractions. The cyan and magenta lines illustrate the 5% and 95% fiber volume fraction values determined from microscopy data of a deconsolidated sample.	30

ABSTRACT

The demand for high quality materials in the aerospace industry has led to continuous aligned fiber composites to be a popular choice in many applications. However, these materials suffer from high costs and manufacturing restrictions. In addressing these problems, aligned discontinuous fiber composites (ADFCs) are being evaluated as an alternative. The relatively recent development of these composites has resulted in a gap in literature regarding fiber direction deformation. The work herein develops a model to predict the extensional deformation of ADFCs for a given microstructure. From a selected matrix material, known fiber geometries, and a desired fiber volume fraction, extensional viscosity is predicted as a function of temperature and strain rate. Model validation was conducted with uniaxial stretch tests on a single ply of thermoplastic matrix AFDC in the fiber direction. These tests implemented digital image correlation techniques to accurately measure strain and inform microstructural nonuniformity. Using this method, experimental extensional viscosity was compared to the model for known input parameters. The model is comprised of a piecewise Newtonian and shear thinning viscosity prediction. Relaxing constituent material assumptions and improving the Newtonian and shear thinning regimes for the polymer were considered to align observations with the model. Implementing these methods was shown to successful bound extensional viscosity data. Nevertheless, the start of the shear thinning regime was not accurately predicted by the model. Further investigation of porosity and fiber reorientation is suggested to explore possible explanations for early onset shear thinning.

Chapter 1

INTRODUCTION

In recent years, there has been an influx of interest in thermoplastic aligned discontinuous fiber composites (ADFCs) as a means to address manufacturability, cost, and recycling challenges associated with traditional continuous fiber composite materials [1]. Viability of this market is largely dependent on the ability to accelerate processing speeds, retain high fiber alignment, and reduce costs. Currently, slower production rates have caused continuous fiber composites to outperform ADFCs in commercial markets [1]. To meet structural requirements, it is important that fiber alignment is maximized in ADFCs if they are to compete with continuous fiber composites since better alignment yields higher fiber volume fractions and improved structural properties. Due to the use of discontinuous fibers, ADFCs have the ability to dominate the thermoplastic composite market since they allow for improved drapability, forming of complex part geometries, and recycled fiber usage as compared to the current state-of-the-art.

In pursuit of highly aligned discontinuous fiber composites, the Center for Composite Materials at the University of Delaware (UD-CCM) has developed a novel composite material form called Tailored Universal Feedstock for Forming (TuFF) consisting of highly aligned discontinuous fiber plies with fiber volume fractions upwards of 60% and fiber lengths on the scale of 3-7mm [2-4]. Figure 1 shows TuFF from the microstructural view of a single ply up to the macroscopic view of a formed

part. Strength and stiffness of TuFF has shown equivalence to continuous fiber composites [5], exceeding the previous state of the art for ADFCs [2]. When combining these properties with the short fiber nature of the material, which enables impressive fiber direction elongation among other benefits, TuFF presents the potential for innovation in a variety of aerospace applications from thermoforming processes to automated fiber placement and tape laying [6-7].

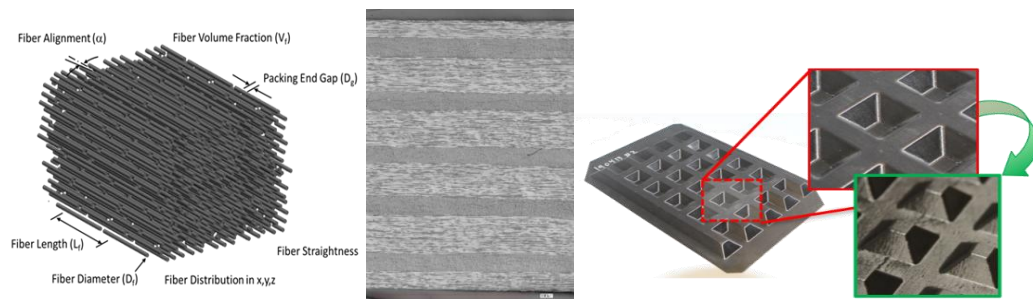


Figure 1. (Left) TuFF fiber scale microstructure [3]. (Center) Cross-section of TuFF laminate structure. (Right) Stretch formed TuFF part [7].

Quasi-isotropic ply sequences, traditionally $[0/45/90/-45]_{ns}$, have previously been used by the UD-CCM to experimentally illustrate TuFF composite formability [7]. However, many aspects of this forming remain unexplored. To better understand the material response to stretch forming, this thesis investigates the extensional viscosity of TuFF composites in the fiber direction and describes the material behavior with constitutive laws. The material form used in this work consists of aligned ~ 3 mm IM7 fibers (aspect ratio of ~ 600) in thermoplastic PEI polymer matrix to produce a composite with $\sim 57\%$ fiber volume fraction. Using digital image correlation (DIC) methods to analyze surface strain patterns, non-uniform sample deformation was

observed. This information provided more accurate strain data when compared to existing methodologies. Operating at strain rates and temperatures indicative of real forming conditions, extensional viscosity was characterized. In addition, a rheological study of the polymer viscosity was conducted using a parallel plate rheometer to characterize the effect of shear rate. This data was fit to Carreau and Spriggs models which describe the behavior of thermoplastic polymers. Finally, a micromechanics model was constructed to relate extensional viscosity of an ADFC with polymer shear viscosity under Newtonian and shear thinning assumptions. Model accuracy was evaluated with respect to the experimentally measured extensional viscosity of the ADFC samples.

There are two main novel contributions of this work. The first is implementation of DIC methods as applied to strain measurement in ADFCs. Material deformation is difficult to assess in short fiber composites due to local nonuniformity. DIC presents an effective and accurate way to inform microstructural properties throughout the deformation process. The second contribution of this work is the development of the predictive micromechanics model. The goal of this work is to understand the specific effects of constituent materials and microstructural parameters in an ADFC which can be generally adopted to new material and microstructure variations. Using this model, the longitudinal deformation of any ADFC can be understood. The material properties and process parameters evaluated in this work will guide material selection and process development for this class of composite materials.

Chapter 2

EXPERIMENTAL METHODOLOGY

2.1 TuFF Sample Preparation

Experimentation of this study was divided into two parts. The first of these methods was stretching in the fiber direction of an ADFC to derive extensional viscosity. This test was performed on single ply, CF-PEI TuFF. Ply parameters were 240 gsm of fiber areal weight (FAW), 254 mm x 254 mm x 0.25mm (10" x 10" x 0.001"), and 57% fiber volume fraction. The constituent materials used were 1) 3 mm IM7 fibers with an aspect ratio of 600 and 2) 0.025 mm (0.0001") thick ULTEM 1000 PEI film. Material fabrication began with a wet-laid process to align precut fibers into a thin-ply with an areal weight of 7.5 gsm [7]. This process results in high fiber alignment (94% of fibers within $\pm 5^\circ$) and is responsible for the high fiber volume fraction achieved. These thin-ply were then hand stacked until the desired prepreg fiber areal weight was reached. After a drying cycle, double-sided film impregnation was performed in an Autoclave under inert atmosphere at 330°C and 300 psi for four hours. The number of film layers was selected to produce blanks with the desired fiber volume fraction.

After resin infusion and consolidation, the blank was cut along the fiber direction into 25.4 mm (1") strips, which were then reduced to ~177.8 mm (7") in length. The dimensions of the samples were selected to allow for 75mm grip-to-grip length during testing (material was gripped with 50 mm end tabs on the top and bottom). Once cut to size, width and thickness were measured at the center cross-section of the sample to obtain more accurate initial sample dimensions. These dimensions would become useful later in the collection of accurate test data. The

center 3” of each sample was then speckled on one side with 0.1 - 1.0 mm dots of high temperature white spray paint with a target surface coverage area of 50%. These speckles enabled local strain measurement across the entire ungripped surface of the sample using digital image correlation methods which are described in Section 5.2. Finally, the samples were left in a drying oven at 120°C for at least 16 hours to remove any trapped moisture prior to testing.

2.2 PEI Rheology

The shear viscosity of the PEI polymer (used in the composite matrix) was measured using a parallel plate rheometer at elevated temperature in an inert atmosphere. As will be shown in Section 3, composite deformation for ADFCs can be predicted based on the shear viscosity of the matrix. Since validation of this model was pursued experimentally, consistent conditioning of all samples was important. To maintain this consistency, the same 0.0001” thick ULTEM 1000 PEI film used in the composite was also tested for this experiment. To prepare the polymer samples for the rheometer, forty layers of film were cut into 6” x 6” sheets and stacked to a thickness of 1 mm, before being consolidated into a single panel in a Carver press at 250°C and 100 psi for thirty minutes. From this panel, 25 mm diameter disks were cut and dried for 24 hours at 120°C. To reproduce the Autoclave thermal cycle, the disks were loaded into the rheometer and held at 330°C for four hours in an inert (N₂ gas) environment. At the end of the hold, five oscillatory frequency sweeps were performed for temperatures of 250°C, 280°C, 300°C, 330°C, and 350°C. Each frequency sweep ranged from 0.1 rad/s to 600 rad/s with a strain amplitude of 0.1%.

2.3 Extensional Viscosity Testing

Characterization of composite deformation was conducted in the fiber direction under uniaxial tension. Isothermal, constant strain rate conditions were imposed using a Universal Test Machine (UTM Instron 4484) and environmental chamber. Temperatures of 300°C, 330°C, and 350°C were investigated along with strain rates ranging from 10^{-5} s^{-1} to 10^{-2} s^{-1} . All of these temperatures were above the glass transition temperature of PEI ($T_g=217 \text{ C}$), therefore viscous deformation was expected. Each sample was initially loaded into the grips with the speckled portion facing outward. A window in the environmental chamber enabled image capture for surface strain measurement. Grip-to-grip length was measured to apply the desired strain rate and then the chamber was closed to begin heating. After steady state temperature was reached, an axial displacement ramp was applied, followed by a displacement hold. In the ramp portion, the sample was stretched at a constant true strain rate. A stop condition was placed at $\epsilon_L = 0.1$, determined from the initial sample length. Once the stop condition was reached, a 100 second hold period commenced to observe stress relaxation in the sample and validate the assumption that the material is only viscous (no elastic strain). Polymer and extensional experiment setups are shown in the Appendix.

Chapter 3

PREDICTIVE MICROMECHANICS MODEL

The construction of a generalized model for aligned discontinuous fiber composites presents a valuable opportunity to understand the principles contributing to deformation in the fiber direction. The model developed here is an analytical framework developed to predict extensional viscosity from the matrix and microstructure of an ADFC. The unit cell of this model consists of a cylindrical fiber encapsulated by a matrix tube to create a cylindrical unit cell. Both constituent materials have length, L . The fiber has a radius of R_i and diameter d , whereas the polymer has inner and outer radii of R_i and R_o respectively. For simplification, the fiber is treated as a rigid rod-like body, whereas the polymer behaves as a viscous fluid. The contribution of fiber end-to-end gaps is not considered. As a result, fiber ends are assumed touching and an average overlap length $L/2$ is used between neighboring fibers. Figure 1 shows a normal view of two neighboring unit cells.

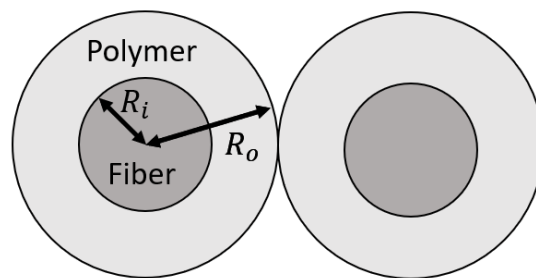


Figure 2. Cross-sectional view of two neighboring unit cells, each consisting of a single fiber of radius R_i encompassed by a polymer of thickness $R_o - R_i$.

3.1 Shape Factor

Although a cylindrical unit cell allows for a simple model, the packing of cylinders is not representative of a real, nonporous composite. Simplifying the unit cell to a 2D cross-section like that shown in Figure 2, the densest possible packing orientation for an inscribed circle is hexagonal. Under this scenario, 9% of material is discarded (see Figure 3 for reference) as it falls outside of the boundary of the cylinder. This wasted material is increased further for square packing. To represent true volume fraction more accurately within the cylindrical unit cell model, shape factors were implemented for square and hexagonal packing. These values were used to calculate true fiber packing as shown in Equation 1. The shape factors for these different packing orientations are provided below in Figure 3.

$$V_f = \frac{1}{\beta} \left(\frac{R_i}{R_o} \right)^2 \quad (1)$$

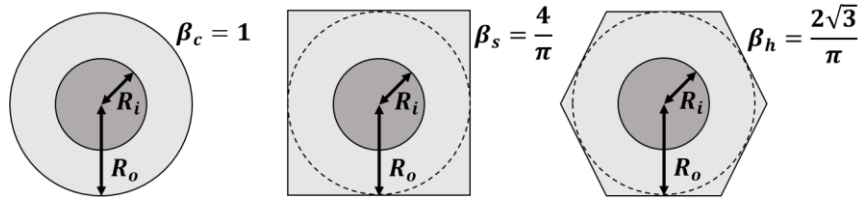


Figure 3. Shape factors for three different unit cell cross-sections. The fiber is shown in dark gray and the matrix in light gray.

3.2 Model Set Up

For the problem at hand, unidirectional loading in the fiber direction is of interest. This was represented with an applied strain, ϵ_L , in the longitudinal (fiber) direction of the composite. To determine the velocity of fibers, the centerpoint was used. Given the assumed average fiber overlap of $L/2$, the relative velocity of

neighboring fibers is $\Delta v_z = \frac{\dot{\epsilon}_L L}{2}$, where z indicates the fiber direction. As seen in Figure 4, relative velocity between fibers does not tell us about the velocity at the boundary between unit cells. To resolve this issue, a reference plane $z = 0$ is placed along the point of rotational symmetry about the boundary of neighboring unit cells. This plane is a vertical distance $L/4$ from either fiber centerpoint, hence the relative velocities of the two adjacent fibers with respect to the reference plane is $\pm \frac{\dot{\epsilon}_L L}{4}$.

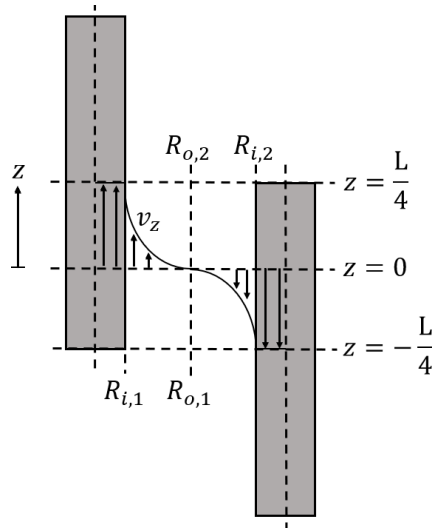


Figure 4. Front view of two neighboring cells. Velocity profile, v_z , is displayed relative to a symmetric neutral axis, $z = 0$, corresponding to a vertical distance of $L/4$ from either fiber end. The boundary conditions at the fiber and unit cell surfaces are $v_z(r = R_o) = 0$ and $v_z(r = R_i) = \pm \frac{\dot{\epsilon}_L L}{4}$ respectively.

3.3 Newtonian Unit Cell Model

The goal of this model is to describe a relationship between polymer viscosity and composite extensional viscosity. Thermoplastic polymers are known to exhibit Newtonian and shear thinning behavior depending on the shear rate of the polymer. Based on experimental observations described in Section 4, both regimes were

deemed valuable for practical forming rates of thermoplastic composites. To apply an analytical model, these assumptions must be applied separately. In general, the relationship between extensional viscosity and longitudinal strain rate is described by Equation 2. When considering polymer viscosity under Newtonian assumptions, behavior is described by Equation 3.

$$\eta_L = \frac{\sigma_L}{\dot{\epsilon}_L} \quad (2)$$

$$\eta_p = \frac{\tau}{\dot{\gamma}} \quad (3)$$

Combining these equations, relative viscosity (η_L/η_p) is shown below.

$$\frac{\eta_L}{\eta_p} = \frac{\sigma_L \dot{\gamma}}{\tau \dot{\epsilon}_L} \quad (4)$$

Polymer shear rate was determined from the cylindrical Navier-Stokes equations, implementing the following assumptions for the unit cell: incompressibility, no-slip conditions at the fiber surface, and one-dimensional, steady flow. From these assumptions, the governing equation was determined (Equation 5).

$$\nabla \cdot \tau = \frac{\partial}{\partial r} \left(r \frac{\partial v_z}{\partial r} \right) \Big|_{r=R_i} = 0 \quad (5)$$

This was then used alongside boundary conditions (Equations 6 and 7) to obtain shear rate (Equation 8).

$$v_z(r = R_o) = 0 \quad (6)$$

$$v_z(r = R_i) = \frac{\dot{\epsilon}_L}{4} \quad (7)$$

$$\dot{\gamma} = \frac{\dot{\epsilon}_L}{2 \ln \sqrt{\beta V_f}} \frac{L}{d} \quad (8)$$

A relation between shear and normal stress within the unit cell was then derived using a force balance. Figure 5 provides a visual representation of the forces on one half of the unit cell in response to extension. The relationship is provided in Equation 9.

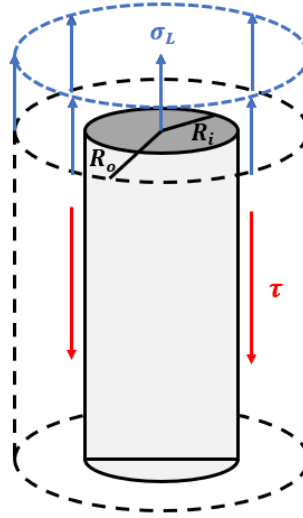


Figure 5. Tensile stress is applied normally to the unit cell of interest, hence acting on an area of $A_\sigma = \pi R_o^2$. In the other direction, shear stress acts on the fiber surface, with area $A_\tau = \pi R_i L$. From these, a force balance can be conducted in the z-direction.

$$\frac{\sigma_L}{\tau} = -2\beta V_f \frac{L}{d} \quad (9)$$

From Equations 8 and 9, relative viscosity was determined as shown in Equation 10.

This equation differs from a previous similar model by a factor of four [9].

$$\frac{\eta_L}{\eta_p} = -\frac{\beta V_f}{\ln \sqrt{\beta V_f}} \left(\frac{L}{d}\right)^2 \quad (10)$$

3.4 Shear Thinning Unit Cell Model

Application of the shear thinning model is slightly more involved. Under these conditions, the polymer follows power law behavior (Equation 11). The flow

consistency index, K , is described in Equation 12. From these equations, polymer and extensional viscosity is related in Equation 13.

$$\eta_p = K\dot{\gamma}^{n-1} \quad (11)$$

$$\ln(K) = \ln(\eta_p) - (n - 1)\ln(\dot{\gamma}) \quad (12)$$

$$\eta_L = K \frac{\sigma_L \dot{\gamma}^n}{\tau \dot{\epsilon}_L} \quad (13)$$

Applying the same assumptions as in the previous section under shear thinning behavior results in the following relation between shear and strain rate.

$$\dot{\gamma} = \frac{\dot{\epsilon}_L}{2} \frac{1-n}{n} \frac{L}{d} \left[1 - (\beta V_f)^{\frac{1-n}{2n}} \right]^{-1} \quad (14)$$

Using the same force balance from Equation 9, the shear thinning extensional viscosity model is developed.

$$\eta_L = K \left(\frac{\dot{\epsilon}_L}{2} \right)^{n-1} \left(\frac{1-n}{n} \right)^n \left(\frac{L}{d} \right)^{n+1} (\beta V_f)^{\frac{n+1}{2}} \left[(\beta V_f)^{\frac{n-1}{2n}} - 1 \right]^{-n} \quad (15)$$

3.5 Applying Newtonian and Shear Thinning Regimes

The analytical structure of this model should only be applied to complete shear thinning and complete Newtonian regimes. However, the unit cell model defines shear rate on the fiber surface, which is the maximum shear rate within the cell. As a result, complete shear thinning behavior will not be observed throughout the unit cell shear rate is marginally greater than the lower bound, $1/\lambda$. To account for this, the cutoff for the shear thinning regime must be adjusted such that the cutoff is applied for $\dot{\gamma}_{min} > 1/\lambda$ as opposed to $\dot{\gamma}_{max} > 1/\lambda$. Equation 16 shows the relationship between $\dot{\gamma}_{max}$ and $\dot{\gamma}_{min}$.

$$\frac{\dot{\gamma}_{max}}{\dot{\gamma}_{min}} = (\beta V_f)^{\frac{-1}{2n}} \quad (16)$$

Chapter 4

POLYMER CHARACTERIZATION

4.1 Rheology Data

As shown in the previous section, the value of this model is in providing a direct relationship between polymer and composite. Verifying the accuracy of this model allows for the prediction of fiber direction stretching for any highly aligned, high fiber volume fraction composite given knowledge of the matrix material and microstructure. The first step in model validation is matrix characterization. The five tests conducted on ULTEM 1000 PEI are shown in Figure 6.

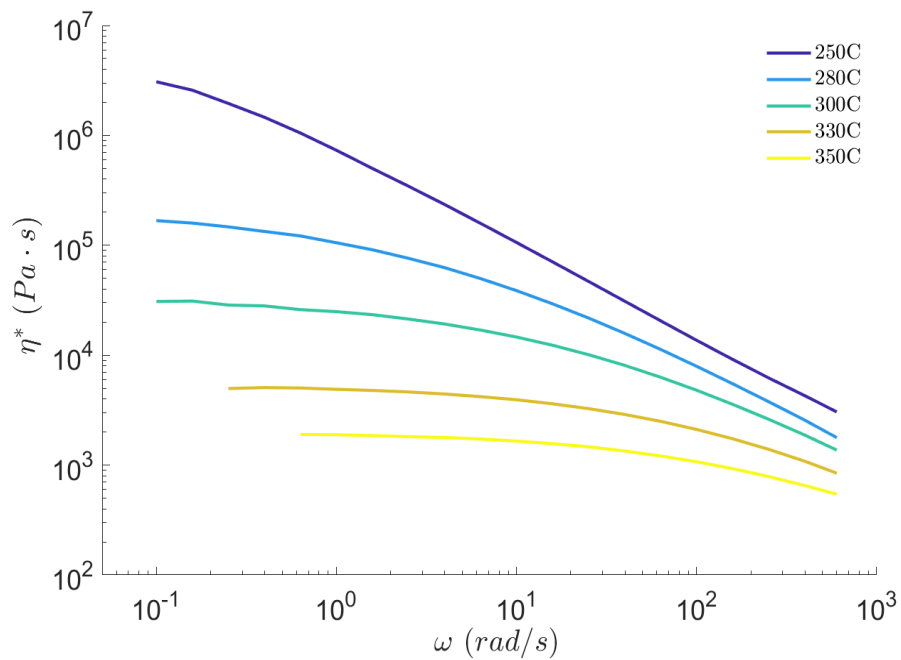


Figure 6. Polymer rheology data for five temperatures under an oscillatory frequency sweep.

4.2 Time-Temperature Superposition (TTS)

Since target forming temperature for CF-PEI TuFF is 330°C, this temperature was used as the baseline for polymer and composite characterization. Using the data collected above, a master curve was constructed using time-temperature superposition with Arrhenius shift factors (a_T and β_T) as described in Equations 17 and 18 below.

Table 1 provides these shift factors.

$$\eta_{T0} = \frac{\eta_T \beta_T}{a_T} \quad (17)$$

$$\dot{\epsilon}_{T0} = \dot{\epsilon}_T a_T \quad (18)$$

Table 1. List of polymer shift factors derived from time-temperature superposition using a baseline temperature of 330°C.

Temperature (°C)	250	280	300	330	350
a_T	3190	40.5	6.25	1.00	0.352
β_T	1.15	1.09	1.05	1.00	0.968

To align with the model constructed in Section 3, polymer data was fit to a Spriggs model as described in Equation 19. This piecewise model allows Newtonian and shear thinning assumptions to be applied separately in their respective acceptable regimes. The data was also fit to a Carreau-Yasuda model (simplified for $\eta_\infty = 0$) described in Equation 20. Figure 7 shows both of these models applied to the PEI master curve at 330°C. Notably, the Carreau-Yasuda model is a near perfect fit whereas the Spriggs model has increasing error approaching the relaxation time. Due to the analytic nature of the extensional viscosity model developed in the previous section, the Spriggs model was used as input, where Newtonian and shear thinning regions were analyzed separately. Fitting parameters for the Spriggs and Carreau models are provided in Table 2.

$$\eta_p = \begin{cases} \eta_0 & \dot{\gamma} \leq 1/\lambda \\ K\dot{\gamma}^{n-1} & \dot{\gamma} > 1/\lambda \end{cases} \quad \text{where } K = \eta_0\lambda^{n-1} \quad (19)$$

$$\eta_p = \eta_0 [1 + (\lambda\dot{\gamma})^a]^{-\frac{n-1}{a}} \quad (20)$$

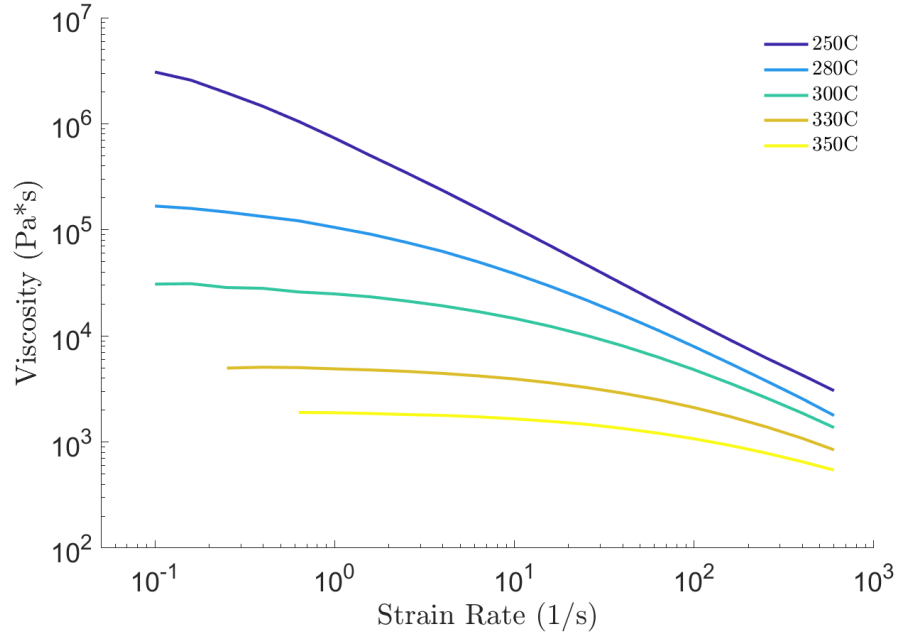


Figure 7. Master curve constructed with time-temperature superposition (TTS) from experimental data shown alongside Carreau-Yasuda and Spriggs models.

Table 2. List of ULTEM 1000 PEI material parameters for the Spriggs and Carreau-Yasuda models at 330°C.

η_0 (Pa · s)	λ (s)	n	a
5200	0.0094	0.13	0.65

Chapter 5

EXTENSIONAL VISCOSITY

The model in Section 3 enables extensional viscosity to be predicted as a function of η_p , V_f , and $\frac{L}{d}$. Given the data collected in the previous section, all this information is known. To validate the accuracy of the model, uniaxial fiber direction stretching was performed to experimentally characterize a composite with known constituent properties.

5.1 Viscous Behavior

Since the polymer is in the melt phase at forming temperatures, the composite is presumed to deform viscously. The unit cell model treats the polymer as a carrier fluid consisting of suspended fibers. In applying ramp-hold conditions to the composite, strain-rate response can be understood and used to inform this hypothesis. Figure 8 below shows the stress response of one sample under longitudinal deformation. At around the 80 second mark, the hold portion of the test initiated with the sample reaching $\varepsilon_L = 0.1$. Stress relaxed to zero, validating our treatment of the composite as a viscous fluid. This was observed across all tests.

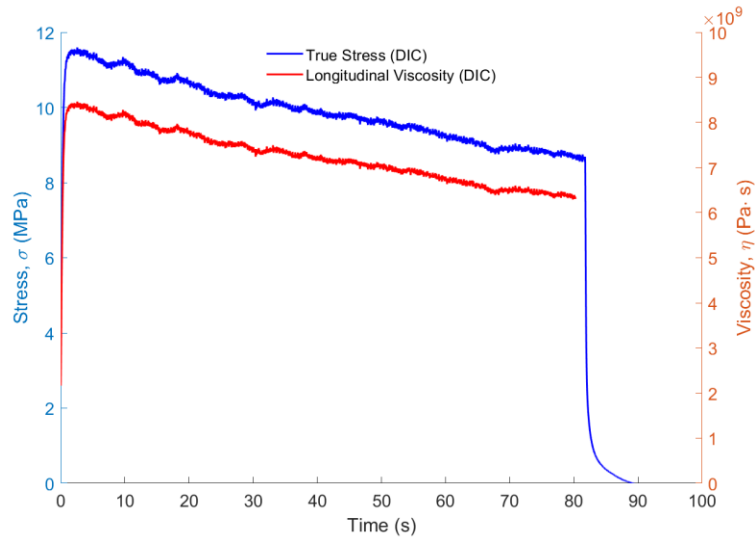


Figure 8. Stress and viscosity versus strain for a sample under baseline conditions of 330°C and 0.001 s^{-1} . As seen in blue, stress relaxes to zero when stretching stops. This suggests the composite behaves viscously.

5.2 Digital Image Correlation (DIC)

One of the key metrics used to define viscosity was longitudinal true strain, ϵ_L . Both σ_L and $\dot{\epsilon}_L$ are strain dependent, therefore accurate measurement is crucial to collecting accurate viscosity data. There are several common methods for measuring tensile strain experimentally including direct displacement measurement and the use of strain gauges. Both techniques are insufficient for ADFCs. Direct displacement of the machine crosshead considers the entire length of a specimen as the gauge length. In doing so, the longitudinal strain gradient is ignored, leading to underestimates of the sample strain. Reducing the gauge length through the introduction of a strain gauge improves upon the issue described. However, this method fails to consider microstructural variability resulting from nonuniform fiber packing, alignment, end gaps, and overlaps. Each of these factors can have a considerable impact on the deformation response and can lead to localized regions of low or high strain. It is

desirable to determine an appropriate gauge length that represents a global average strain for the specimen while also observing the local variability due to the fluctuation of microstructural differences throughout samples. To address each of these issue, digital image correlation (DIC) analysis was implemented to collect local strain data across the surface of samples. A video extensometer was used to take approximately 200 images of the speckled sample surface throughout the duration of each test. DIC analysis was conducted in VIC2D. Images were analyzed with a subset size of 41 pixels and a step size of 2. Each pixel length was approximately 0.051 mm, resulting in subsets with a size of 2.08 mm x 2.08 mm. From there, true strain was calculated at each subset in the sample to create a surface strain map. This strain map was used to determine appropriate dimensions for the sample gauge section. Figure 9 shows the selected dimensions and region for one sample.



Figure 9. Visualization of gauge section determined using DIC methods. Sample dimensions were $L_o = 3''$ and $w_o = 1''$, whereas gauge section dimensions were $L_{gauge} = 1''$ and $w_{gauge} = 0.4''$.

The gauge length was reduced from 3” to 1” to avoid effects from the grips, whereas the gauge width was reduced from 1” to 0.4” to avoid sample edge effects. The strain map also informed local variability. As seen within the gauge section, local regions of high strain on the order of one to two fiber lengths were observed. Since these strain localizations were not accurate representations of macroscopic behavior, the gauge length was also selected to be longer than any local extremes.

One concern during testing was the onset of failure. DIC analysis provides a mechanism to observe failure based on strain localization. If high strain regions become more pronounced throughout the duration of a test, this indicates a region of weakness that can lead to failure. Figure 10 shows the evolution of surface strain in one sample from an average strain of $\epsilon_{gauge} = 0.01$ to $\epsilon_{gauge} = 0.08$. The strain map was held consistent throughout, ranging from zero to $1.5\epsilon_{gauge}$.

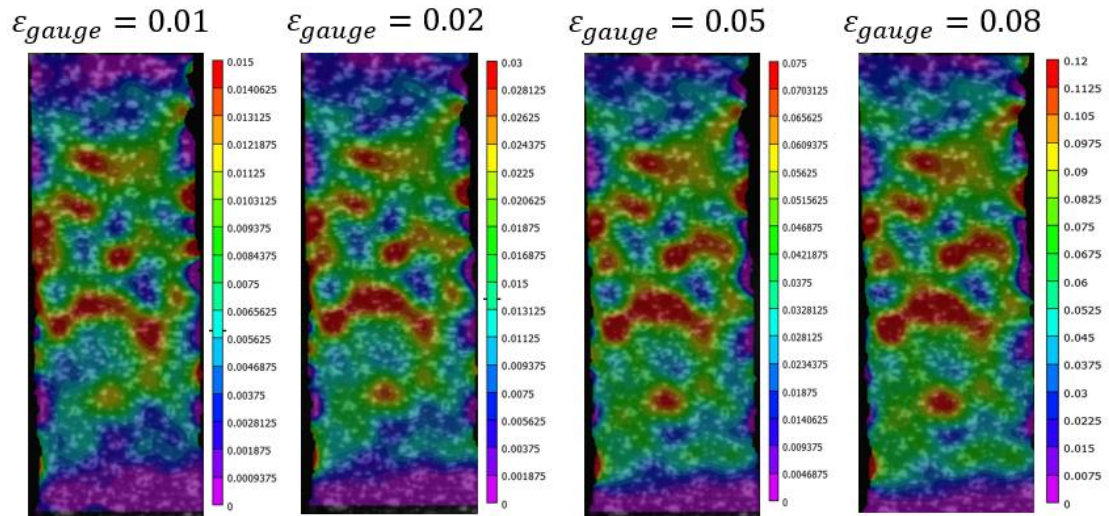


Figure 10. Evolution of local surface strain with average gauge strain using DIC methods for a single test at 350°C and 0.0002 s^{-1} . Using a scale from zero strain to $1.5\epsilon_{gauge}$, minimal localization is observed.

It is clear from Figure 10 that strain localization is minor. The strain map shows minimal change throughout the test in relation to average gauge section strain. Since the regions of high and low strain remained consistent, tearing did not occur within the sample. This is further emphasized by Figure 11, which shows the variability of strain within the gauge section of the sample.

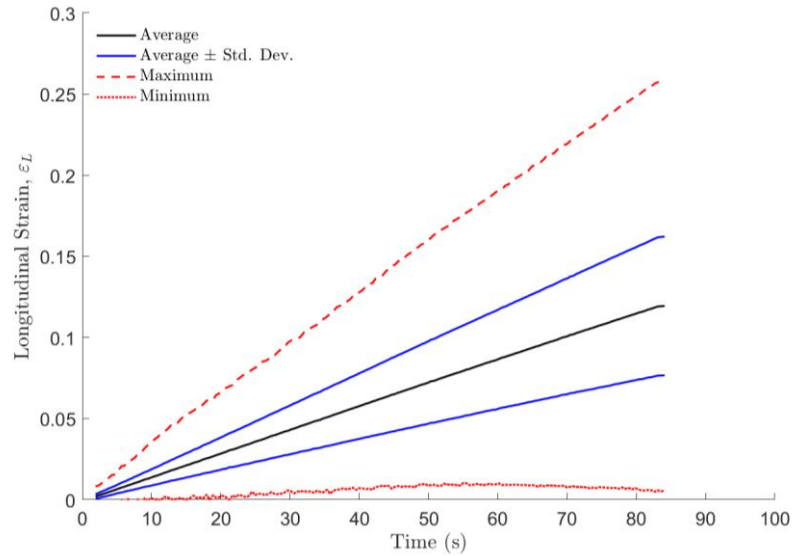


Figure 11. Variability in gauge section strain for a single test at 330°C and 0.001 s⁻¹.

While the maximum and minimum points are about three standard deviations from the gauge section average, this gap is consistent throughout the test. If the sample were to tear, the maximum strain would significantly increase relative to the gauge section average since strain would localize at the region of failure. The absence of this behavior confirms tearing did not occur in this sample. Nevertheless, within the gauge section, strain fluctuated immensely, ranging from about zero to 0.25 when the average was about 0.1. This shows the drastic effects of microstructure on strain

locally. The maxima and minima are likely the result of a high number of subsets within the sample, resulting in the occasional outlier. For the purposes of assessing strain variability, standard deviation is a better judge.

5.3 Temperature and Strain Rate Dependence

Viscous behavior depends on several factor. Both temperature and strain rate are known to have significant impacts on extensional viscosity. However, sample strain also affects viscosity based on the evolution of stress. Since longitudinal elongation results in transverse contraction for an incompressible, transversely isotropic material, stress can be calculated from longitudinal strain. Using this relation, viscosity was measured as a function of strain, strain rate, and temperature. Strain and strain rate were calculated from DIC using the average strain of the gauge section. Multiple tests were then compiled to determine the influence of each of these factors. Figure 12 shows the influence of strain and strain rate on viscosity. On the left, repeatability is shown for baseline test conditions of 330°C and 0.001 s⁻¹.

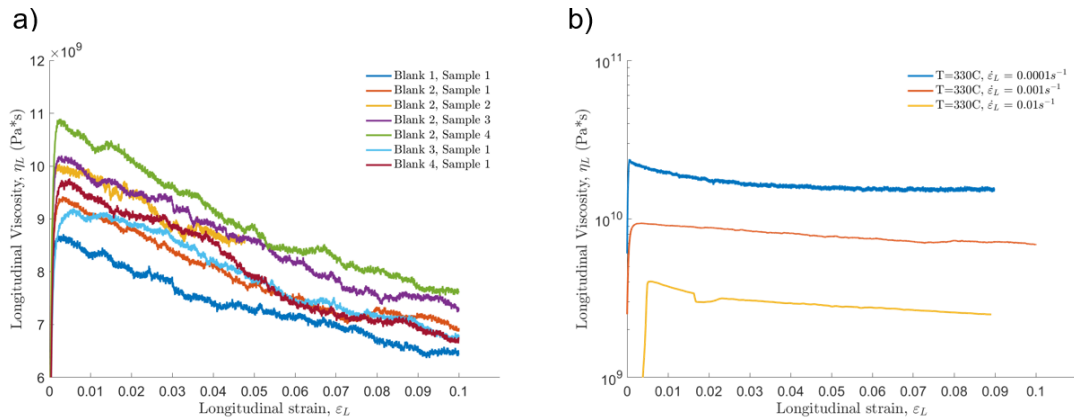


Figure 12. a) All seven tests under baseline conditions of 330°C and 0.001 s⁻¹. b) Viscosity dependence on strain rate and strain using a logarithmic scale.

Seven tests were conducted at this condition across multiple blanks to observe variation in material quality. From this view, strain appears to considerably affect viscosity, causing a 25% decrease from $\varepsilon_L = 0$ to $\varepsilon_L = 0.1$. On the right, different strain rate conditions were investigated at 330°C. This graph shows viscosity on a logarithmic scale and illustrates the much more pronounced effect of strain rate compared to strain. The red curve in both graphs represent the same test. On the left, the 25% decrease in viscosity appears significant, while on the right, it is nearly imperceptible. Given the greater effect of strain rate than strain, viscosity data for each test was simplified to only consider the effects of temperature and strain rate. An average viscosity from $\varepsilon_L = 0.01$ to $\varepsilon_L = 0.02$ was calculated to represent each test.

5.4 Repeatability

To verify the accuracy of methodology and data, it was important to repeat specific test conditions. The baseline condition was repeated seven times as shown above to assess consistency in processing quality and data reduction. After calculating the representative strain rate and viscosity for each test, a single data point was set to the average of the seven tests, with error bars of ± 2 standard deviations for both strain rate and viscosity. The error bars in Figure 13 shows repeatability for multiple test conditions. The fluctuations at each point are minor compared to the effects of temperature and strain rate, indicating consistent methodology and material quality.

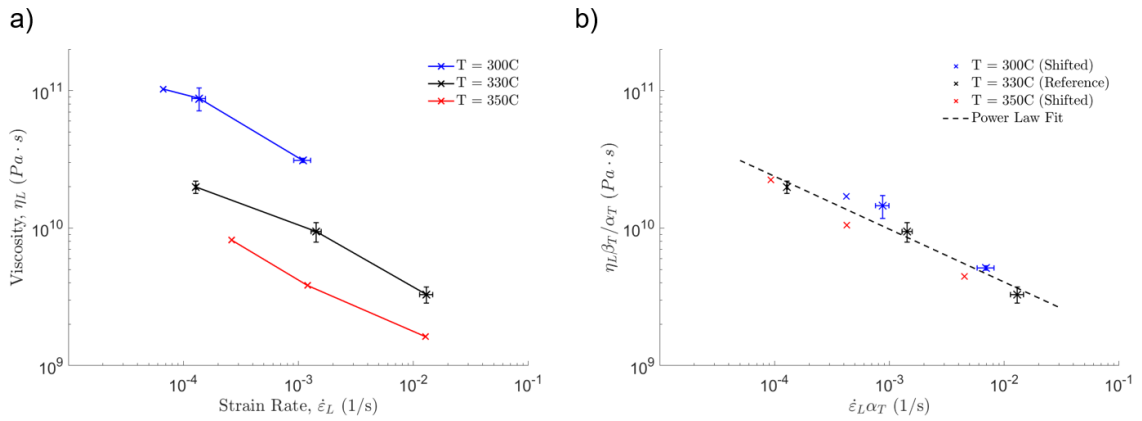


Figure 13. a) Raw viscosity data for three temperatures at strain rates from 0.00005 s^{-1} to 0.01 s^{-1} . Error bars indicate ± 2 standard deviations in both strain rate and viscosity across identical test conditions. b) TTS shifted composite data fit to a power law model. Power law parameters were $n = 0.62$ and $k = 6.88 \cdot 10^8 \text{ Pa} \cdot \text{s}^n$.

5.5 Test Data

With the representative viscosity determined (from Section 5.3), temperature and strain rate dependence were quantified. Samples were tested at 300, 330, and 350C at strain rates between 10^{-5} s^{-1} and $5 \cdot 10^{-2} \text{ s}^{-1}$. Inaccurate test data points were removed based on sample failure or instrument accuracy limits. Material failure was described by any sample which exhibited observable tearing or excessive strain localization. Figure 14 shows the contrast between passing and failing samples. Measurement failure was described as any test which exhibited either a minimum force below 2% of the maximum load cell rating or an applied strain rate variability greater than 10%. Once failing tests were filtered, passing tests were grouped into isothermal curves as seen in Figure 13a.

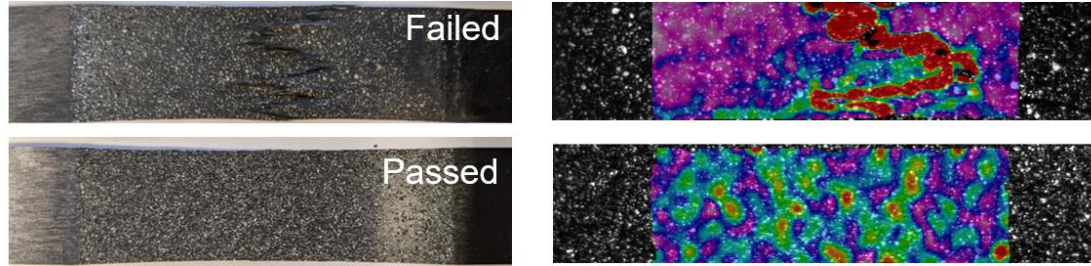


Figure 14. (Top) Sample and DIC strain map for a failing sample stretched at $5 \cdot 10^{-2} \text{ s}^{-1}$. The jagged break in the speckle pattern indicates tearing. This is mirrored by the strain localization across the sample surface shown in the DIC strain map. (Bottom) Sample and DIC strain map for a passing sample stretched at 10^{-3} s^{-1} . The uniform DIC pattern indicates that tearing did not occur.

Since these same temperatures were studied during polymer characterization, the TTS shift factors from Table 1 were applied to the composite to construct a ‘composite master curve’ as seen in Figure 13b. After shifting, the data appeared to closely follow a linear profile, although the onset of an observable Newtonian plateau appears possible at the lower strain rate. Nevertheless, a power law fluid model was applied to the data to approximate the power law index aligning with shear thinning behavior.

5.6 Application of Predictive Model

From the model and experimental data, a prediction of composite viscosity was formulated. The polymer parameters described in Table 2 were used alongside micromechanical parameters of $\frac{L}{a} = 600$ and $V_f = 57\%$ (hexagonal packing) as inputs to the model. This prediction was then compared to the TTS shifted experimental data provided in the previous figure to produce Figure 15. The green and black lines come from the polymer master curve and Spriggs model respectively. The Newtonian and shear thinning regimes were then shifted independently to predict extensional

viscosity as seen in blue and red. The gap in these regions is defined by the application of the shear thinning assumptions described in Section 3.5. All experimental data was shown to exist in the Newtonian regime but behaved slightly shear thinning. Additionally, the Newtonian plateau, while not fully observed experimentally, is clearly underpredicted by the model. These issues are addressed in the next section.

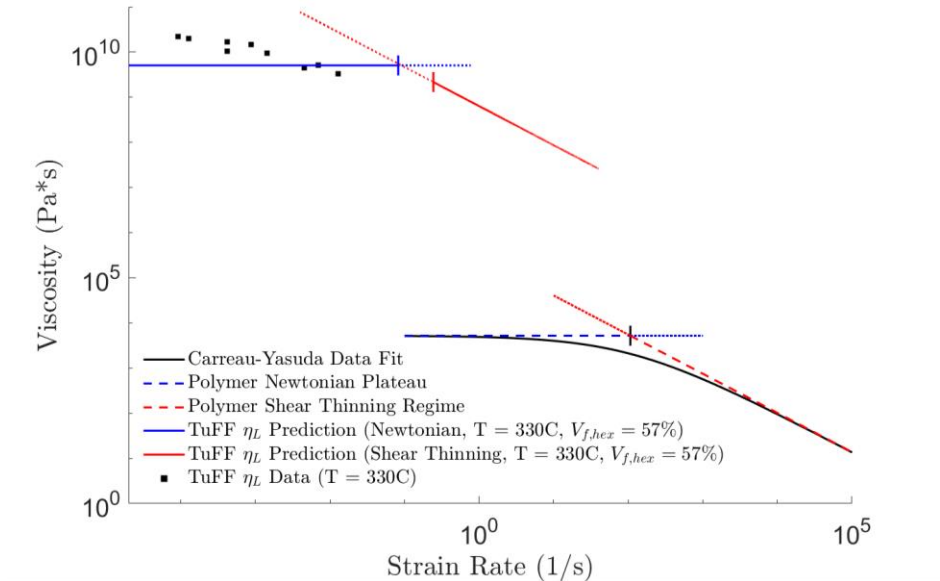


Figure 15. Piecewise model prediction applied to TuFF data in the Newtonian (blue) and shear thinning (red) regimes.

Chapter 6

DISCUSSION

6.1 Model Accuracy

It is clear from Figure 15 that the model failed to accurately predict extensional viscosity data. While the prediction is close to observed values, there are two main issues with the fit of the model: 1) the onset of shear thinning is poorly predicted by the model, and 2) the observed Newtonian plateau is underpredicted. These issues are addressed below in order.

6.1.1 Shear Thinning Behavior

The limitations of this model are apparent from the Newtonian and shear thinning inputs derived from the Spriggs model for the polymer. The limitation of the piecewise Spriggs model is accuracy in the transition zone, where the model overpredicts the polymer viscosity. The Carreau-Yasuda model clearly shows the weakness of this assumption; at $\dot{\gamma} = 1/\lambda$, the Spriggs prediction is more than double what is observed. From Figure 15, it is apparent that the entire range is not needed for composites, as the higher shear rates are unattainable for forming. Reducing this range to only the lower shear rates which are representative for forming can alter the slope of the shear thinning regime, improving the accuracy of the piecewise model at these lower rates.

To reduce the scope of the piecewise model, the observed TuFF power law index was used to approximate a power law model to the polymer shear viscosity data in the transitions zone. Matching the power law indices, an upper bound within the polymer was selected where $n' = 0.62$ (the power law index for observed TuFF data). This value was used to back solve for a new relaxation time, which would adjust the

Newtonian and shear thinning regimes. Figure 16 shows this new power law approximation applied to the polymer, where the solid lines indicate the region of interest. This adjustment improves the model by shifting the shear thinning regime to the left and improving the overall accuracy of the Newtonian and shear thinning input conditions.

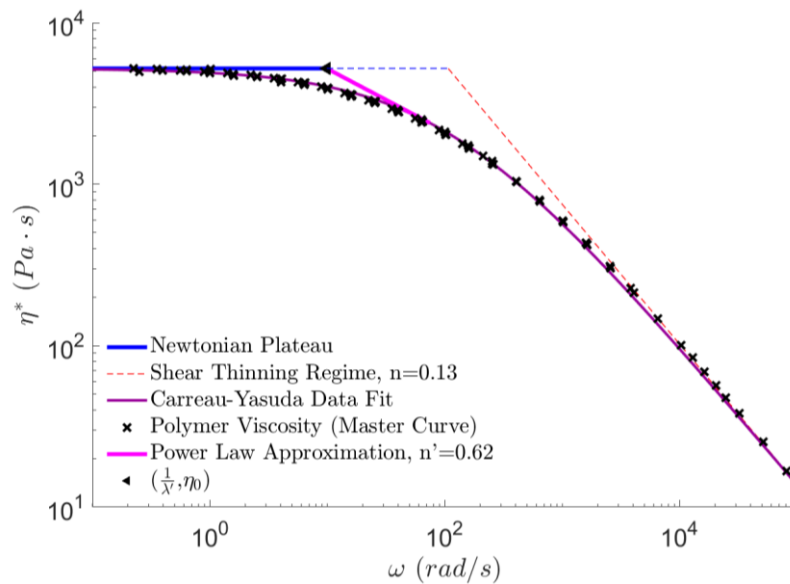


Figure 16. Revised model to incorporate a power law approximation that aligns with the behavior observed in the composite. The solid lines indicate the region within which forming rates are observed. The better alignment between the new region and the Carreau fit indicates improved model input accuracy.

6.1.2 Newtonian Plateau

With the shear thinning issue addressed, relative viscosity must be adjusted to predict the Newtonian plateau more accurately. Ideally, the plateau would be easily identifiable from the extensional viscosity data. Unfortunately, the plateau was not clearly observed due to limitations in testing capability. Nevertheless, the relatively

shallow slope at the lower shear rates of Figures 13 and 15 indicates a likely plateau. As a result, the zero-shear viscosity was assumed at the experimental maximum viscosity data point observed. Using this value, the model underpredicts the plateau viscosity by an order of magnitude. To align the model with observations, input parameters, namely fiber volume fraction and aspect ratio, were adjusted to bound observations.

Within the composite, the microstructure was observed to vary greatly. From microscopy studies, local fiber volume fraction was shown to follow a normal distribution centered at 58% with a standard deviation of 8% as seen in Figure 17. A one standard deviation range sets a reasonable bound for macroscopic behavior. Additionally, the possibility of a different packing structure, namely square, is a possible explanation for higher-than-expected viscosity. Both factors were considered in constructing an appropriate prediction range.

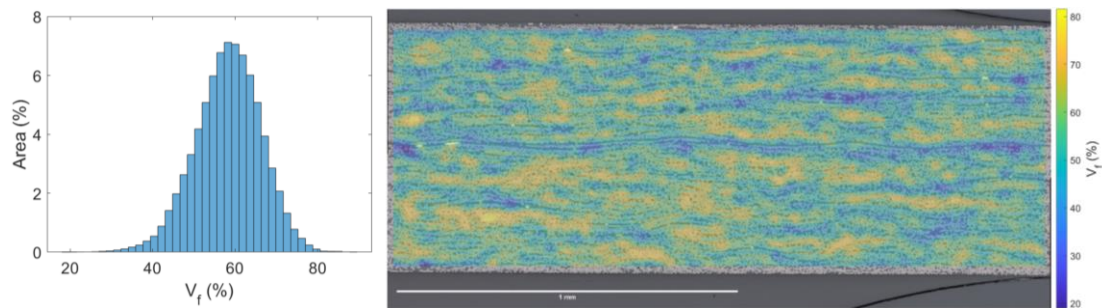


Figure 17. (Left) Histogram of local volume fraction data. Data fits a normal distribution centered at $V_f = 58\%$ with a standard deviation of 8%. (Right) Colormap of local fiber volume fraction across a deconsolidated sample from microscopy.

Fiber aspect ratio assumptions can also be relaxed to alter the model prediction. Previous inspection of fiber length and diameter have been conducted to assess the variability of these quantities within the prepreg and coupon [3]. Length and diameter had respective coefficients of variation of 10% and 5%, centered about 3mm and $4.77\mu\text{m}$ ($5.03\mu\text{m}$ for prepreg). Accounting for one standard deviation in length and diameter variability, observed aspect ratio fluctuates between 530 and 740. This range was also implemented to predict material behavior.

6.2 Revised Model Prediction

The adjustments described above allow for improved input values as well as relaxed assumptions. The bounding range was kept small enough for the model to provide predictive value, but large enough to allow for plausible variability in microstructure and constituent material geometries. Figure 18 shows the adjusted model for low, average, and high predictions. Notably, adjustments in volume fraction and aspect ratio provided an appropriate upper bound for predicting the Newtonian plateau.

While the onset of shear thinning was improved, the model is still horizontally shifted by approximately an order of magnitude. A horizontal shift factor could be applied for a given set of input parameters, but this option was not pursued to avoid the use of fitting parameters. There are several possible explanations for the early onset of shear thinning. A likely explanation is oversimplification. The model developed in Section 3 leverages several important assumptions, namely perfect alignment, no fiber end gaps, and rigidity of fibers. The effect of fiber misalignment on strain rate response lacks understanding and could show strong interdependence. Likewise, the modeling of fibers neglects bending, which could alter longitudinal strain response. Finally, the model ignores fiber end gaps. Depending on the size of these gaps, they could

contribute to several effects, such as lower cross-sectional fiber volume fractions (although this is disputed by microscopy data) as well as fiber clustering or end alignment. Any or all these effects could contribute to the underpredicted horizontal and vertical shifts of the polymer.

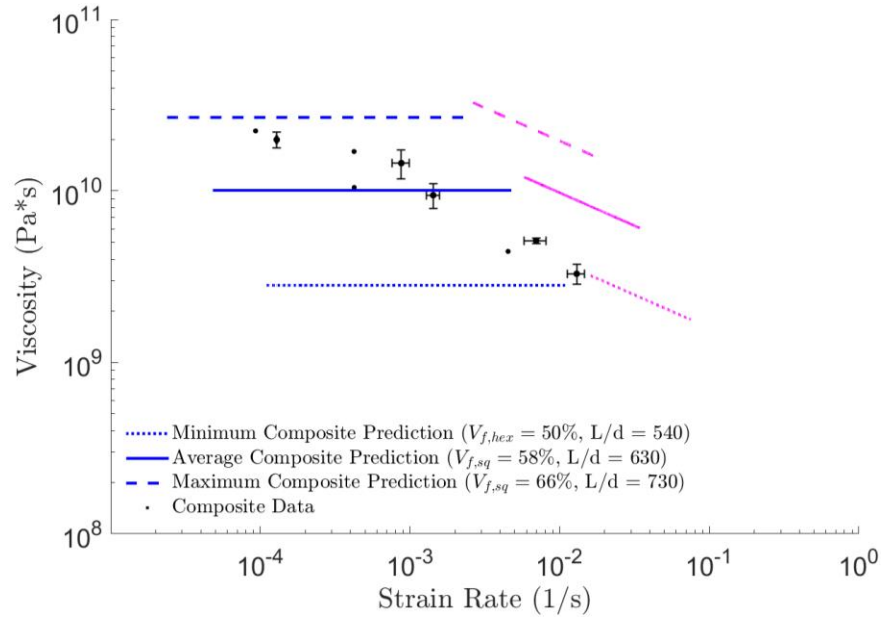


Figure 18. Model predictions compared to TuFF data for varying fiber volume fractions. The cyan and magenta lines illustrate the 5% and 95% fiber volume fraction values determined from microscopy data of a deconsolidated sample.

Chapter 7

CONCLUSIONS

Aligned discontinuous fiber composites (ADFCs) present an opportunity for the development of complex, high-quality composite forms that are cheaper and faster to manufacture when compared to the industry standard. The youth of this technology demands further understanding of deformation in the fiber direction. This work develops a process for accurately characterizing the material response of an ADFC with known parameters. Given the unique challenge in understanding global behavior due to microstructural variability, digital image correlation (DIC) was used to analyze local deformation across entire samples. This data informed local variability while also assisting in the selection of a gauge section that accurately represented tests. This method improves upon existing experimental methods and provides specific value for ADFCs due to their inherently high nonuniformity.

The other goal of this work was the development of a robust but simple micromechanics model. This model is intended to predict extensional viscosity for any ADFC given knowledge of the microstructure and matrix material. Applying this model to tests conducted herein provided a basis on which to assess its accuracy. From average material parameters, the model was shown to slightly underpredict observed viscosity. Using microscopy data from other work, fiber volume fraction assumptions were relaxed and used to bound the model prediction. In doing so, experimental extensional viscosity was successfully encapsulated, with the upper limits in fiber volume fraction accurately predicting the Newtonian plateau.

Moving forward, further investigation of ADFCs should focus on uniformity in microstructure and deformation response. A deeper understanding of the connection

between local strain response and microstructure is valuable in optimizing material design and forming conditions. Additionally, for complete characterization of ADFCs, porosity effects and transverse behavior should be studied further under multi-directional loading.

NOMENCLATURE

a	Carreau-Yasuda fitting parameter
a_T	Horizontal shift factor
A_σ	Cross-sectional area through which normal stress acts
A_τ	Surface area of unit cell on which shear stress acts
β_T	Vertical shift factor
β	Shape factor
$\dot{\gamma}$	Shear rate
$\dot{\gamma}_{max}$	Maximum shear rate in a unit cell
$\dot{\gamma}_{min}$	Minimum shear rate in a unit cell
d	Fiber diameter
ε_{gauge}	Average longitudinal strain within the gauge section
ε_L	Longitudinal true strain
$\dot{\varepsilon}_L$	Longitudinal true strain rate
$\dot{\varepsilon}_T$	Longitudinal true strain rate at some temperature T
$\dot{\varepsilon}_{T0}$	Longitudinal true strain rate at baseline temperature, 330°C
η_0	Zero-shear viscosity of polymer
η_L	Longitudinal viscosity of composite
η_p	Polymer shear viscosity
η_T	Longitudinal viscosity of composite at some temperature T
η_{T0}	Longitudinal viscosity of composite at baseline temperature, 330°C
K	Flow consistency index
L	Length of fiber
L_{gauge}	Gauge length of sample

L_o	Grip-to-grip length of sample
λ	Relaxation time
n	Power law index
R_i	Radius of fiber
R_o	Radius of unit cell
σ_L	Longitudinal stress of composite
τ	Shear stress of polymer
w_{gauge}	Gauge width of sample
w_o	Width of sample
v_z	Velocity in the z-direction
V_f	Fiber volume fraction

REFERENCES

1. SUCH, M., WARD, C., & POTTER, K. (2014). Aligned Discontinuous Fibre Composites: A Short History. *Journal of Multifunctional Composites*, 2(3), 155–168. <https://doi.org/10.12783/issn.2168-4286/2/3/4>
2. Yarlagadda, S., Deitzel, J., Heider, D., Tierney, J., & Gillespie, J. W. (2019). *TAILORABLE UNIVERSAL FEEDSTOCK FOR FORMING (TUFF): OVERVIEW AND PERFORMANCE*.
3. Heider, D., Tierney, J., Henchir, M. A., Gargitter, V., Yarlagadda, S., Gillespie, J. W., Sun, J., Sietins, J. M., & Knorr, D. (2019). *MICROSTRUCTURAL EVALUATION OF ALIGNED, SHORT FIBER TUFF MATERIAL*.
4. Heider, D., Tierney, J., Deitzel, J., Kubota, M., Thiravong, J., Gargitter, V., Burris, W., Morris, J., Shevchenko, N., Yarlagadda, S., & Gillespie, J. W. (2019). *CLOSED LOOP RECYCLING OF CFRP INTO HIGHLY ALIGNED HIGH PERFORMANCE SHORT FIBER COMPOSITES USING THE TUFF PROCESS*.
5. Hexcel 8552 IM7 Unidirectional Prepreg 190 gsm & 35%RC Qualification Material Property Data Report FAA Special Project Number SP4614WI-Q Test Panel Fabrication Facility. (2019). https://www.wichita.edu/industry_and_defense/NIAR/Documents/Qual-CAM-RP-2009-015-Rev-B-Hexcel-8552-IM7-MPDR-04.16.19.pdf
6. Revolutionizing Aircraft Materials and Processes. (2020). In *Revolutionizing Aircraft Materials and Processes*. Springer International Publishing. <https://doi.org/10.1007/978-3-030-35346-9>
7. Yarlagadda, S., Advani, S., Deitzel, J., Heider, D., Molligan, D., Roseman, D., Simacek, P., Tierney, J., & Gillespie, J. W. (2019). *FORMABILITY OF TUFF COMPOSITE BLANKS*.
8. Šimáček, P., & Advani, S. G. (2019). A micromechanics model to predict extensional viscosity of aligned long discontinuous fiber suspensions. *International Journal of Material Forming*, 12(5), 777–791. <https://doi.org/10.1007/s12289-018-1447-y>
9. Creasy, T. S., & Advani, S. G. (1997). A model long-discontinuous-fiber filled thermoplastic melt in extensional flow. *Journal of Non-Newtonian Fluid Mechanics*, 73(3), 261–278. [https://doi.org/10.1016/S0377-0257\(97\)00045-1](https://doi.org/10.1016/S0377-0257(97)00045-1)

APPENDIX

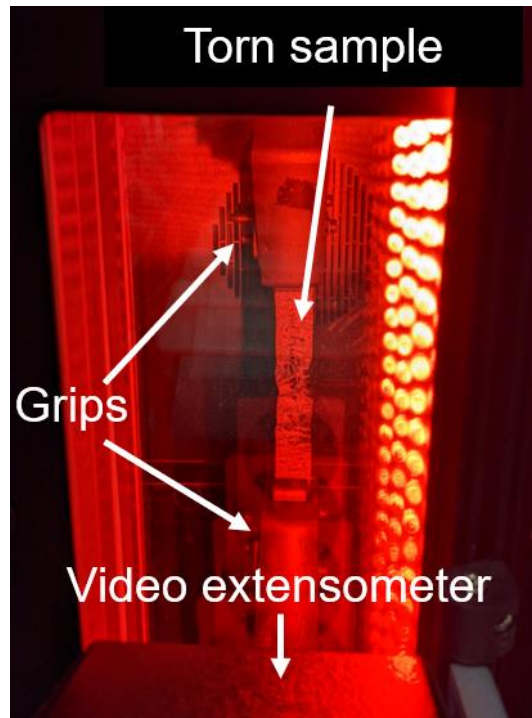


Figure A1. View of a uniaxial stretch test on a speckled sample within an environmental chamber. The top grip moves upwards based on the imparted strain rate from the UTM crosshead to stretch the sample. The video extensometer is used to take pictures of the sample throughout the duration of the test in order to collect strain data.



Figure A2. Polymer rheology setup with 25 mm diameter, 1 mm PEI disk loaded between two parallel plates.